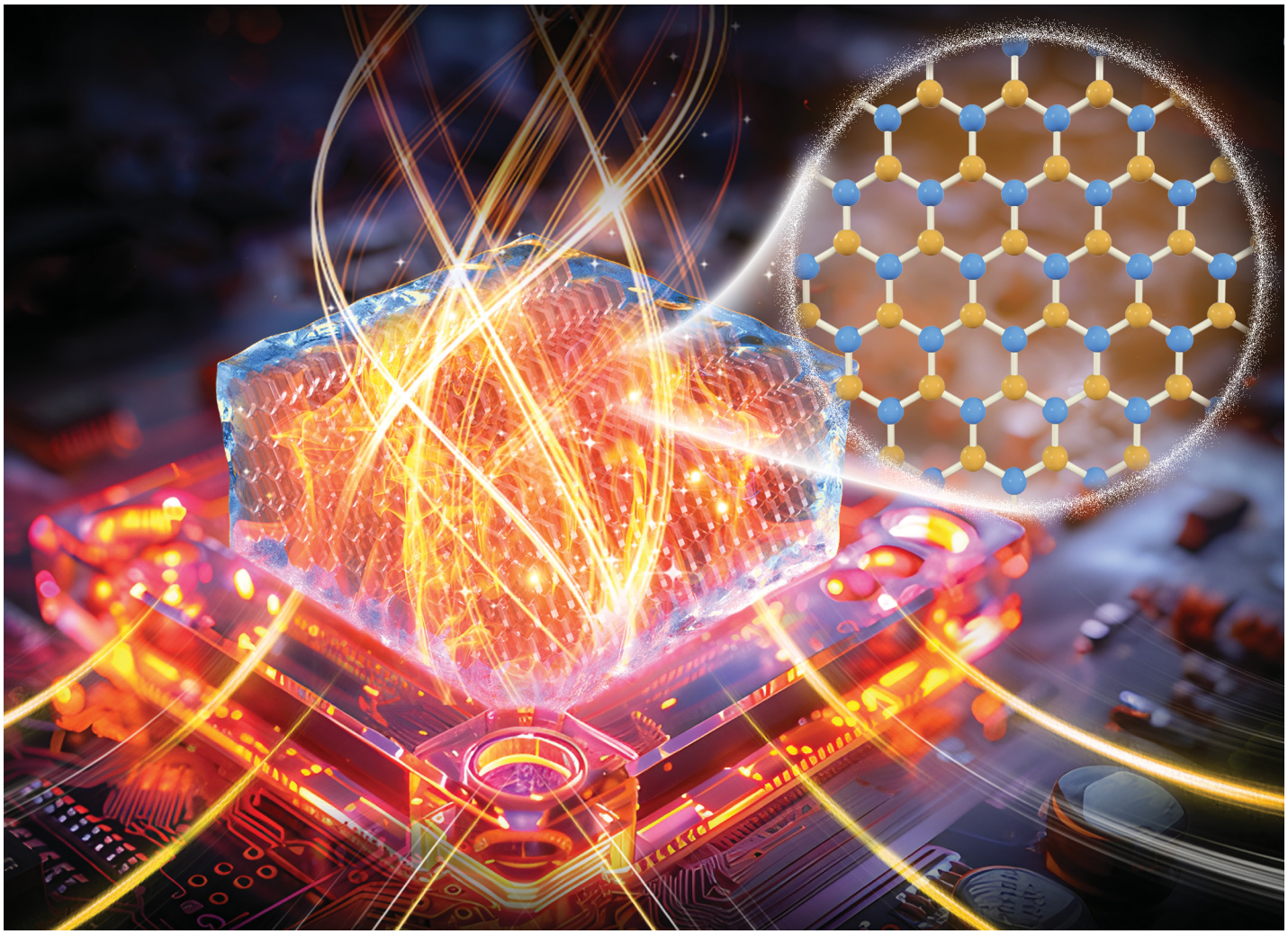

Showcasing research from Professor Jinhong Yu's research group at the Key Laboratory of Advanced Marine Materials, Ningbo Institute of Materials Technology and Engineering, Chinese Academy of Sciences, Ningbo, China.

Highly oriented BN-based TIMs with high through-plane thermal conductivity and low compression modulus

Successive implementation of techniques such as stacking, densifying, and vertical cutting resulted in the development of a remarkable BN-based TIM. This TIM is characterized by outstanding thermal conductivity, notably low compression modulus and total effective thermal resistance. This pioneering feat contributes valuable technical insights for the development of high performance insulating TIMs.

As featured in:

See Chen Xue, Jinhong Yu *et al.*, *Mater. Horiz.*, 2024, **11**, 4064.

ROYAL SOCIETY OF CHEMISTRY

rsc.li/materials-horizons

Registered charity number: 207890

Materials Horizons

ROYAL SOCIETY OF CHEMISTRY

COMMUNICATION

View Article Online
View Journal | View Issue

Cite this: *Mater. Horiz.*, 2024, 11, 4064

Received 22nd May 2024,
Accepted 16th July 2024

DOI: 10.1039/d4mh00626g

rsc.li/materials-horizons

Highly oriented BN-based TIMs with high through-plane thermal conductivity and low compression modulus†

Rongjie Yang,[ab] Yandong Wang,[a] Zhenbang Zhang,[a] Kang Xu,[a] Linhong Li,[ab] Yong Cao,[c] Maohua Li,[a] Jianxiang Zhang,[a] Yue Qin,[a] Boda Zhu,[ab] Yingying Guo,[a] Yiwei Zhou,[a] Tao Cai,[a] Cheng-Te Lin,[ab] Kazuhito Nishimura,[a] Chen Xue,*[a] Nan Jiang[ab] and Jinhong Yu*[ab]

In the pursuit of effective thermal management for electronic devices, it is crucial to develop insulation thermal interface materials (TIMs) that exhibit exceptional through-plane thermal conductivity, low thermal resistance, and minimal compression modulus. Boron nitride (BN), given its outstanding thermal conduction and insulation properties, has garnered significant attention as a potential material for this purpose. However, previously reported BN-based composites have consistently demonstrated through-plane thermal conductivity below 10 W m^{-1} K^{-1} and high compression modulus, whilst also presenting challenges in terms of mass production. In this study, low molecular weight polydimethylsiloxane (PDMS) and large-size BN were utilized as the foundational materials. Utilizing a rolling-curing integrated apparatus, we successfully accomplished the continuous preparation of large-sized, high-adhesion BN films. Subsequent implementation of stacking, cold pressing, and vertical cutting techniques enabled the attainment of a remarkable BN-based TIM, characterized by an unprecedented through-plane thermal conductivity of up to 12.11 W m^{-1} K^{-1}, remarkably low compression modulus (55 kPa), and total effective thermal resistance (0.16 °C in^2 W^{-1}, 50 Psi). During the TIMs performance evaluation, our TIMs demonstrated superior heat dissipation capabilities compared with commercial TIMs. At a heating power density of 40 W cm^{-2}, the steady-state temperature of the ceramic heating element was found to be 7 °C lower than that of the commercial TIMs. This pioneering feat not only contributes valuable technical insights for the development of high-performance insulating TIMs but also establishes a solid foundation for widespread implementation in thermal management applications across a range of electronic devices.

New concepts

The advancement of high-power density electronic devices has necessitated enhanced performance of insulation thermal interface materials (TIMs). Addressing the urgent need for TIMs with high through-plane thermal conductivity and remarkably low compression modulus is of paramount importance. In this study, we employed polydimethylsiloxane (PDMS) and large-sized boron nitride (BN) in conjunction with an innovative roller curing process to facilitate the continuous production of high-adhension BN/PDMS films. Successive implementation of techniques such as stacking, densifying, and vertical cutting resulted in the development of a remarkable BN-based TIM. This TIM is characterized by outstanding through-plane thermal conductivity, notably low compression modulus and total effective thermal resistance. Compared to the state-of-the-art commercial TIMs, the BN-based TIM exhibits superior thermal dissipation capabilities, suggesting a wider range of potential applications in electronic thermal management. As a proof of concept, this research demonstrates an efficacious strategy for the large-scale production of high-performance thermal interface materials.

1. Introduction

As technological advancements persist, emerging fields such as artificial intelligence, 5G communication, and quantum computing impose progressively rigorous demands on device performance.[1] High-performance devices typically display compact designs and elevated power density, which consequently generate considerable heat during operation, necessitating increasingly effective thermal management. Among various thermal management materials, thermal interface materials (TIMs)[2,3] serve a crucial role in enhancing heat transfer efficiency by filling microscopic gaps between heat sources and

[a] *Key Laboratory of Advanced Marine Materials, Ningbo Institute of Materials Technology and Engineering, Chinese Academy of Sciences, Ningbo, China. E-mail: xuechen@nimte.ac.cn, yujinhong@nimte.ac.cn*

[b] *Center of Materials Science and Optoelectronics Engineering, University of Chinese Academy of Sciences, Beijing 100049, China*

[c] *State Key Lab of Materials Processing and Die & Mould Technology, School of Materials Science and Engineering, Huazhong University of Science and Technology, Wuhan, 430074, China*

† Electronic supplementary information (ESI) available. See DOI: https://doi.org/10.1039/d4mh00626g

heat sinks, primarily improving heat conduction in the thickness direction. Currently, TIMs predominantly comprise polymer matrices filled with thermally conductive fillers, exemplified by graphene,[4–6] carbon fibres,[7–9] and metal.[10–12] Despite remarkable progress in thermal conductivity, conductive-filler-based TIMs frequently exhibit insufficient insulation properties and risk of electrical short circuits, potentially resulting in equipment damage. Conversely, TIMs with superior insulation performance, commonly developed by incorporating Al_2O_3,[13,14] have encountered subpar thermal conduction performance and struggle to meet evolving application requirements. Consequently, there is an urgent need for emerging TIMs that demonstrate high through-plane thermal conductivity and exceptional insulation properties.

The emerging hexagonal boron nitride (h-BN),[15,16] which shares a similar two-dimensional crystalline structure with graphite, has been demonstrated to achieve high thermal conductivity comparable to that of pure aluminium. Simultaneously, in contrast to the erratic C–C bonds in graphene, the B–N bonds endow h-BN with remarkable insulation property. Regrettably, due to the hexagonal lattice structure, BN exhibits high thermal conductivity anisotropy between the in-plane and through-plane directions. This intrinsic issue presents significant obstacles for researchers in efficiently enhancing the thermal conductivity of polymer matrices with BN.

In order to fully harness the exceptional in-plane thermal conductivity of BN, a variety of techniques, such as mechanical orientation, vacuum filtration, and hot processing, are being developed for the fabrication of thermally conductive polymer films.[17–20] By increasing the BNNS filler content to 50 wt%, the thermal conductivity of BNNS/cellulose nanofiber films can be significantly enhanced to 24.6 W m^{-1} K^{-1} following shear-induced orientation.[21] Moreover, a substantially higher thermal conductivity of 73.3 W m^{-1} K^{-1} can be attained by raising the BNNS loading to 85 wt% and employing tape casting and vacuum hot-pressing methods.[22]

Although considerable progress has been made in the development of high thermal conductivity films, the production of dielectric insulation BN-based composites with superior through-plane thermal conductivity remains a formidable challenge. While techniques such as electric[23,24] and magnetic fields,[25,26] as well as freeze-drying,[27,28] can facilitate vertical alignment, they are not amenable to large-scale production due to scalability constraints. Consequently, the strategy of winding or stacking horizontally oriented thin sheets, followed by vertical cutting to achieve BN vertical arrangement, offers a promising avenue for widespread application. For instance, Yin *et al.* reported a roll-cutting method to obtain MVQ/ABN composites with vertically aligned boron nitride, and show a maximum thermal conductivity of 6.3 W m^{-1} K^{-1}.[29] Hu *et al.* fabricated a silicone rubber-based composites with high through-plane thermal conductivity of 7.62 W m^{-1} K^{-1} and softness prepared by combining shear orientation and layer-by-layer stacking methods.[30] However, preparing large-sized BN-based composites with through-plane thermal conductivity exceeding 10 W m^{-1} K^{-1} and compressive modulus below 1 MPa remains a huge challenge.

In this study, we proposed a scalable method for producing large-sized BN composites with high through-plane thermal conductivity. By employing roller curing integrated equipment, we continuously fabricated BN/polydimethylsiloxane (PDMS) films characterized by superior horizontal orientation and excellent adhesion properties. Upon stacking and cold pressing these films, vertically oriented BN composites can be prepared. With 75 wt% BN filling, the vertically oriented BN/PDMS composites displayed a through-plane thermal conductivity of 12.11 W m^{-1} K^{-1}, surpassing that of most previously reported BN/BNNS-based composites. The exceptional structure and high flexibility of PDMS resulted in an extremely low compressive modulus of 55 kPa and a total effective thermal resistance of 0.16 °C in^2 W^{-1}. In practical thermal management applications, the vertically oriented BN/PDMS composite exhibited superior heat dissipation performance compared to commercial TIMs. These results offer promising implications for the advancement of high-performance insulating TIMs in industrial applications.

2. Experimental section

2.1. Materials

Hexagonal boron nitride (h-BN) was purchased from Foshan Daoning Chemical Industry Co., Ltd, China (Fig. S1, ESI†). For simplicity, h-BN is referred to as BN. The modified polydimethylsiloxane (PDMS) employed was provided by Shenzhen Hong Fu Cheng Co., Ltd, China. The commercially available insulating TIM (WT5902, k = 9 W m^{-1} K^{-1}) was obtained from Tianjin WaermTimo New Material Technology Co., Ltd, China. The commercial graphene thermal pad was purchased from Shanghai Zihong electric Industry Co., Ltd, China. Invar alloy (4J36, 11 W m^{-1} K^{-1}) was purchased from Dongguan Changan Mingshang metal material trading firm.

2.2. Preparation of BN/PDMS composites (dough, film, and Pad)

Initially, BN/PDMS doughs with varying BN loadings were prepared using a high-speed mixer (SpeedMixer, FlackTek, Germany). For instance, to create a BN/PDMS dough with 75 wt% BN content, 45 g BN powders were combined with 15 g PDMS (A : B = 1 : 1) and mixed at 2000 rpm for 5 min. Subsequently, the BN/PDMS dough was placed on a conveyor belt and passed through double rollers, with PET film attached to the top and bottom surfaces of the dough. The roller distance was set at 0.3 mm. The in-plane oriented BN/PDMS film was then cured for 6 hours at 85 °C on a heating stage. Following this, the cured BN/PDMS film was cut into 30 × 28 mm^2 flakes using customized cutting tools, and the flakes were stacked within the cutting tools. The stacked flakes were then placed into a mold, and a pressure of 6 MPa was applied to the mold's upper and lower surfaces for 2 min at room temperature. Lastly, the densified BN/PDMS composites were vertically cut to obtain pads using an ultrasonic knife. The detailed preparation process is shown in Fig. S2 (ESI†).

2.3. Characterization

The microstructures and morphological features of h-BN and BN/PDMS composites were examined using a scanning electron microscope (HITACHI, SEM Regulus 8230, Japan). The crystallographic properties of BN and BN/PDMS composites were studied using X-ray diffraction (Bruker, D8 Discover/GADDS, Germany) with CuKα radiation. The three-dimensional structure of Pad-75-V was reconstructed from X-ray computed tomography (micro-CT) images using Dragonfly software, and the micro-CT images were captured using an X-ray three-dimensional imaging system (ZEISS, Xradia 610 Versa, Germany).

X-ray diffraction patterns were collected on a 2D Wide-Angle X-ray diffraction instrument (XENOCS SAS, Xeuss 3.0 UHR, France).

The Herman's orientation factor was calculated according to the formula:

$$H = \frac{3}{2}\frac{\int_0^{\pi/2} d\varphi \sin\varphi I(\varphi)\cos^2\varphi}{\int_0^{\pi} d\varphi \sin\varphi I(\varphi)} - \frac{1}{2} \quad (1)$$

where φ is the azimuthal angle and $I(\varphi)$ represents the intensity distribution along with the azimuthal angle φ of the (002) plane.

The thermal conductivity of the composites was calculated using the formula:

$$k = \alpha \times \rho \times C_p \quad (2)$$

where α, ρ, and C_p represent the thermal diffusivity, density, and specific heat capacity of the composites, respectively. The thermal diffusivity α was measured using a laser flash apparatus (NETZSCH, LFA 467, Germany). The specific heat capacity was determined by differential scanning calorimetry (NETZSCH, DSC 214, Germany). The density was obtained based on the Archimedes principle. The thermal resistance was measured using a Longwin 9389 thermal conductivity tester following the ASTM 5470 method. An infrared camera (Fluke, Ti400, USA) was employed to capture IR images. The dielectric properties of the BN/PDMS composites were measured using an LCR meter (TH 2838A, Changzhou Tonghui Electronics Co., Ltd, China) in the frequency range of 10^3 to 10^6 Hz at room temperature. The mechanical properties of BN/PDMS composites were acquired using a universal material testing machine (Zwick, Z030TE + TEE, Germany).

3. Result and discussion

3.1. Preparation and structural characterization of Pad-75-V

BN displays a two-dimensional crystalline structure characterized by a flat and smooth surface, as evidenced by the SEM image shown in Fig. 1a. The crystal structure of BN, depicted in Fig. 1b, resembles a honeycomb, wherein boron and nitrogen atoms are arranged alternately, forming a layered structure similar to graphite. This configuration facilitates enhanced thermal conductivity in the in-plane direction (400 W m^{-1} K^{-1}), contributing to its exceptional in-plane thermal conductivity. However, the weak connections between layers hinder heat conduction in the through-plane direction, resulting in significantly lower through-plane thermal conductivity (30 W m^{-1} K^{-1}).[31] The anisotropic thermal conductivity of BN is evident, as shown in Fig. 1c. Previous attempts at simple blending[32–34] and hot pressing[35–37] have struggled to produce an ordered vertical arrangement structure, leading to ineffective thermal conductivity paths and poor thermal conductivity in the resulting composites. Although the ice-templated method[38–40] can yield an excellent vertical arrangement structure, achieving high BN filling remains a challenge, resulting in discontinuous overlap between BN and negatively impacting heat transfer efficiency, as illustrated in Fig. 1d. To address these limitations, our proposed method achieves both a high BN filling amount and a highly ordered vertical arrangement of BN structure. The preparation process of the BN thermal pad is primarily divided into two stages: (1) preparing a high-viscosity BN/PDMS film and (2) vertically cutting the film after stacking and densification.

Initially, PDMS is mixed with BN to produce a dough-like mixture, wherein BN is randomly distributed, as shown in Fig. 1e. Then, the BN/PDMS films of large size were obtained by placing the mixture onto a conveyor belt and passing through double rollers, resulting in a horizontal arrangement within the PDMS, as illustrated in Fig. 1f–h. And SEM images of BN/PDMS film with varying thicknesses are presented in Fig. S3 (ESI†). X-ray diffraction (XRD) analysis was employed to characterize the orientation of BN within the film. The ratio of diffraction peak intensity of the (002) and (100) crystal planes serve as a measure of the horizontal orientation of BN in the film. As depicted in Fig. 1i, the $I(002)/I(100)$ intensity ratio for the horizontally oriented film (506.6) significantly exceeded that of the random composite (16.2), indicating a pronounced horizontal alignment. In Fig. 1j, it is evident that the cured BN/PDMS film exhibits remarkable adhesion and flexibility. Subsequently, the cured film undergoes cutting and stacking before cold pressing, resulting in a densely packed BN/PDMS composites with elevated horizontal orientation, as illustrated in the schematic diagram in Fig. 1k. The photograph in Fig. 1l emphasizing the potential scalability and mass production capabilities of this manufacturing process. Fig. 1m highlights the excellent processability of the prepared BN/PDMS composites. The composites can be precisely cut into BN thermal pads of varying thicknesses to suit specific requirements. Notably, these thermal pads commendable flexibility and resistance to bending, rendering them suitable for application in irregular interfaces.

To investigate the microstructure of Pad-75-V, we employed SEM to analyse two perpendicular cross-sections. Fig. 2a and b reveal a well-defined vertical arrangement structure throughout the thickness of the sample, with the side of BN completely displayed. In Fig. 2c and d, the layer-by-layer stacking of BN is apparent, allowing for a more detailed presentation of the base surface. This observation underscores the anisotropic nature of BN and validates the precise structuring control achieved in BN/PDMS composites during the preparation process.

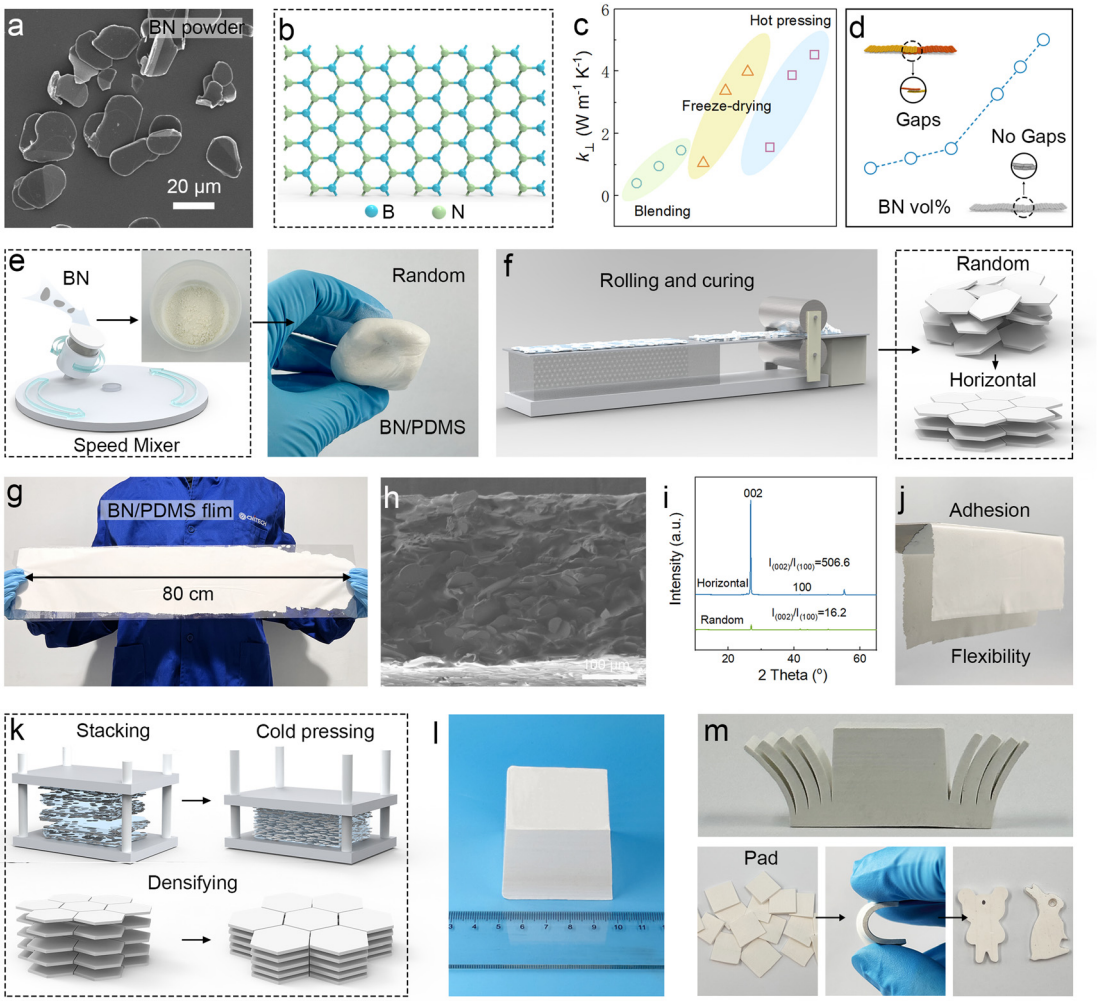

Fig. 1 (a) SEM image showing BN's morphology. (b) Diagram of BN's atomic structure. (c) $K_\perp$ values for BN-based composites using reported methods. (d) Theoretical model representing percolation threshold. (e) BN/PDMS pre-made dispersion preparation. (f) In-plane orientation process. (g) Optical image of the prepared film. (h) Cross-sectional SEM image of the film. (i) XRD results comparing BN/PDMS composites with random and horizontal structures. (j) Optical image displaying film's adhesion and flexibility. (k) Densification process. (l) Large-sized BN/PDMS block. (m) Highly processable BN/PDMS block.

Furthermore, a non-destructive 3D imaging technique micro-CT were employed to provide a finer display of the internal structure of Pad-75-V. The original micro-CT image, as shown in Fig. S4 (ESI†), underwent segmentation techniques in Dragonfly software to generate the three-dimensional diagram and the two-dimensional diagrams in the *xz* and *yz* directions in Fig. 2e. Upon separating BN from PDMS, the vertical arrangement structure of BN, stacked layer by layer in the through-plane direction, becomes more apparent. The continuous overlap of adjacent BN layers forms an efficient thermal conductivity pathway. The observations presented are in line with the SEM images depicted earlier. Furthermore, we devised a model as illustrated in Fig. 2f. In this model, the coordinate system defines the angle θ between BN and the *xy* plane. At $\theta = 90^\circ$, BN is perfectly vertical and appears white, while at $\theta = 0^\circ$, it appears gray. The vast majority of white BN in the micro-CT images confirms the excellent vertical arrangement structure of Pad-75-V. Moreover, we conducted statistical analysis on 72 120 pieces of BN particles within the test block to analyse the distribution of θ. The histogram demonstrates that the range of 75° to 90° encompasses nearly 90% of the sample size, indicating a significant proportion of BN being vertically aligned. Additionally, we quantitatively assessed the orientation degree of Pad-75-V using wide angle X-ray scattering (WAXS). Fig. 2g displays a 2D WAXS image of Pad-75-V, exhibiting a symmetrical circular arc diffraction pattern on the (002) crystal plane. Notably, sharp peaks at 0° and 180° are evident in the Fig. 2h, corresponding to the crystal orientation. By applying the relevant formula, the orientation factor is calculated to be 0.66. In contrast, the diffraction pattern of the random sample assumes a complete circular shape (Fig. 2i), devoid of discernible peaks after fitting (Fig. 2j), and the orientation factor of only 0.14. (Fig. S5, ESI†) These findings collectively underscore the complete and ordered vertical arrangement

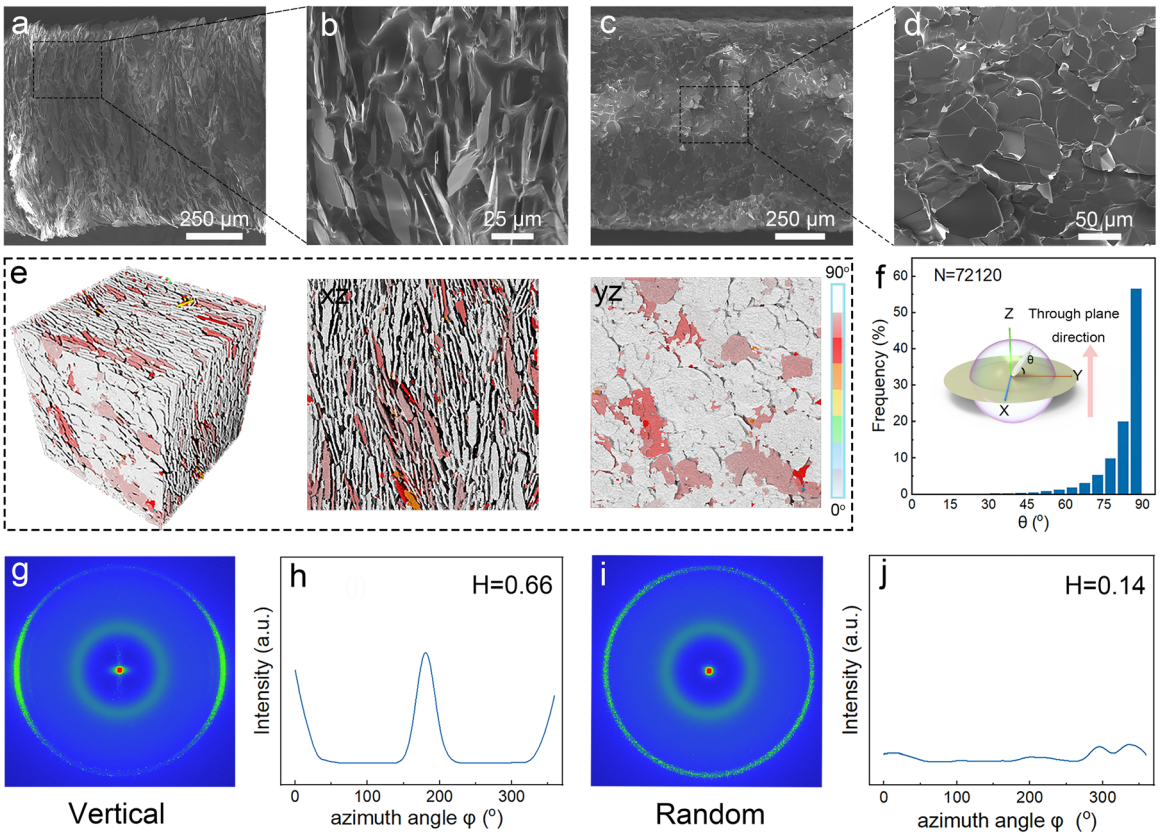

Fig. 2 (a) and (b) SEM images of Pad-75-V from *XZ* view. (c) and (d) SEM images of Pad-75-V from *YZ* view. (e) Reconstructed model with angle distribution of micro-CT result of Pad-75-V. (f) Statistical analysis of angle distribution of BN. (g)–(j) WAXD patterns, azimuth angle curves and Herman's orientation parameters of Pad-75-V and Pad-75-R.

structure of Pad-75-V, providing robust evidence for its outstanding through-plane heat transfer performance.

3.2. Thermal properties

We propose that BN/PDMS composites with vertically aligned, and highly ordered structures exhibit enhanced heat transfer capacity, especially in the vertical direction. To investigate the relationship between the organization of boron nitride and the efficiency of heat transfer, we employed the laser flash method (ASTM 1461) for precise measurements of thermal conductivity in both vertical and horizontal directions. As illustrated in Fig. 3a, the in-plane thermal conductivity of composites, ranging between 60 and 75 wt%, varies from 0.82 to 1.52 W m^{-1} K^{-1}. A discernible increase in thermal conductivity with increasing BN content is observed, but this growth is limited. Meanwhile, the composite material achieves a maximum thermal conductivity of 12.11 W m^{-1} K^{-1} in the through-plane direction. To quantitatively determine the thermal conductivity enhancement in composite materials compared to that of the pure PDMS, we utilized the thermal conductivity enhancement efficiency (TCEE) metric, calculated using the formula:

$$\mathrm{TCEE} = (k_c - k_m)/(k_m \times m_{BN}) \times 100\% \quad (3)$$

where k_c is the thermal conductivity of the composites, and k_m is the thermal conductivity of pure PDMS. As shown in Fig. 3b, the maximum TCEE for BN/PDMS composites (75 wt%) in the in-plane direction is measured at 880%, while in the vertical direction, it reaches a remarkable 7940%. This significant enhancement highlights the effectiveness of vertically aligned BN structures.

Furthermore, in Fig. 3c, the attained through-plane thermal conductivity exceeding 12 W m^{-1} K^{-1} surpasses most reported thermal conductive composite materials based on BN/BNNS, including both disordered[41–45] and vertically arranged structures.[29,30,46–50] To examine the influence of vertically aligned structures on the composites' thermal conductivity, we established models representing BN arranged randomly and vertically, as depicted in Fig. 3d. Subsequent steady-state temperature distribution (Fig. S6, ESI†) analysis (ANSYS) disclosed that composites with vertically aligned structures exhibit considerably enhanced heat transfer efficiency in the through-plane direction compared to those with random structures.

To visually demonstrate the superior through-plane thermal conductivity of Pad-75-V, an experimental setup was devised, as shown in Fig. 3e, comparing it with the Invar alloy. Both Pad-75-V and Invar alloy samples, sized 10 × 10 × 25 mm^3, were placed on a ceramic heating plate. A uniform and dense graphite layer was evenly applied to their upper and lower surfaces to ensure consistent contact and similar infrared emissivity. Using an infrared camera, the surface temperatures

of the two samples were monitored during a 60 s heating process, as depicted in Fig. 3f and g. The results demonstrated that the surface temperature of Pad-75-V consistently remained slightly higher than that of the Invar alloy, indicating the outstanding vertical heat transfer performance of Pad-75-V.

Moreover, considering the practical application of thermal interface materials, an analysis of the association between the thermal conductivity of Pad-75-V and ambient temperature was performed, as shown in Fig. 3h. It was found that as the ambient temperature increased from 25 to 100 °C, the thermal conductivity slightly decreased due to the increased phonon scattering and lattice defects within the crystal material. Nonetheless, the thermal conductivity consistently remained above 10 W m^{-1} K^{-1}, demonstrating that Pad-75-V maintains exceptional heat transfer performance within the typical operating temperature range of electronic devices.

Fig. 3i displays the thermal stability of Pad-75-V during cold and hot cycle testing. After 20 cycles, the deviation of thermal conductivity at 25 and 100 °C is a remarkably low 1.6% and 2.3%, respectively, emphasizing the composite's reliable thermal stability. Additionally, total thermal resistance is an essential metric for assessing the effectiveness of thermal interface materials, commonly determined through steady-state heat flux testing based on the ASTM5470 standard. The testing principle schematic is presented in Fig. 3j. In Fig. 3k, the behavior of total thermal resistance for Pad-75-V at various thicknesses is shown. As test pressure increases, total thermal resistance gradually decreases due to the relationship:

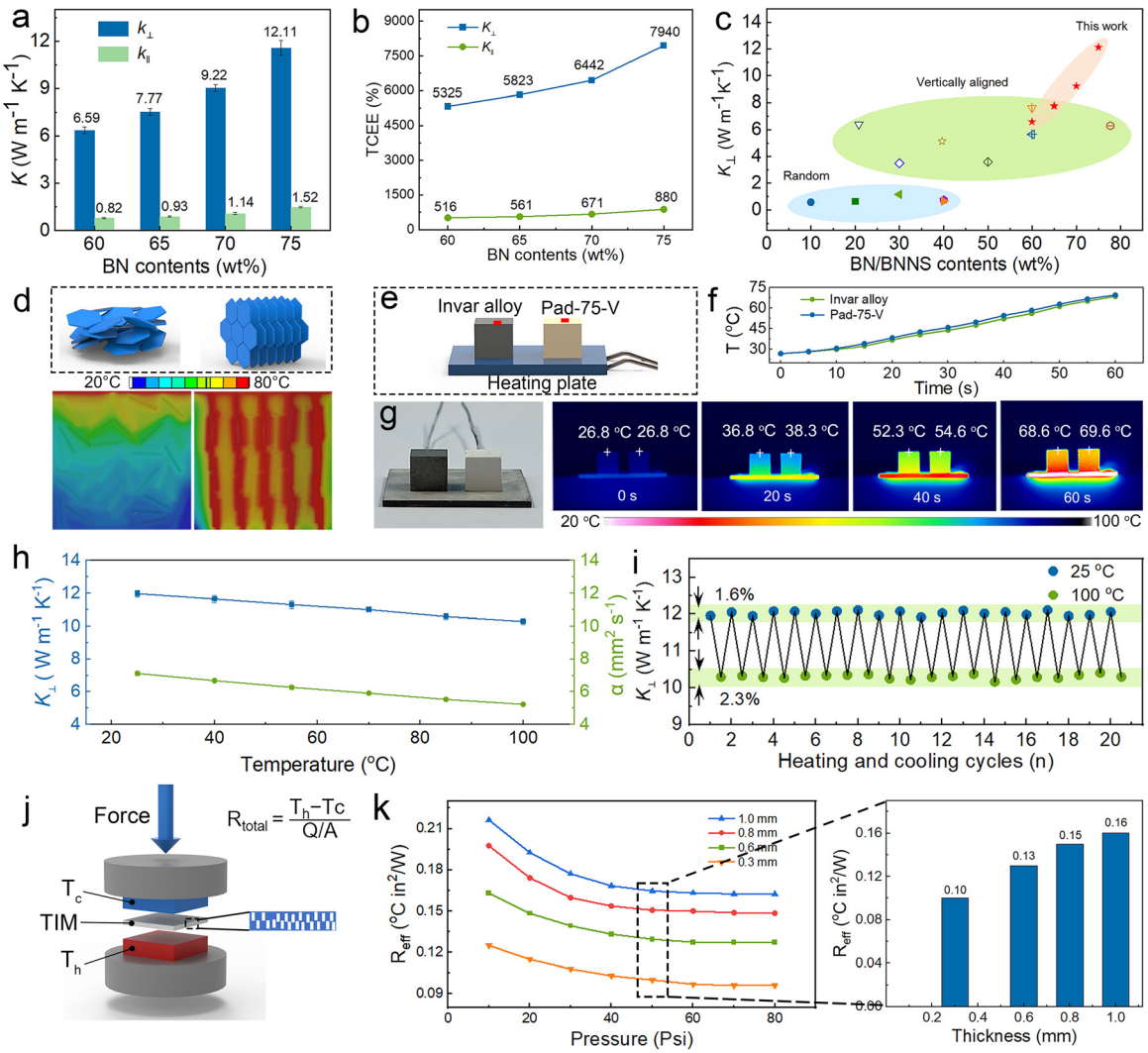

Fig. 3 (a) Thermal conductivity and (b) thermal conductivity enhancement efficiency of anisotropy at various BN contents. (c) Comparison of the $K_{\perp}$ of Pad-75-V with the reported BN/BNNS composites. (d) Simulated transient temperature distribution of BN/PDMS composites with random and vertically aligned structures. (e) The test system for demonstrating the heat transfer capacity along the through-plane direction, with the surface temperature evolution of Invar alloy and Pad-75-V and the IR images shown in (f) and (g), respectively. (h) The $K_{\perp}$ of Pad-75-V as a function of environmental temperature and (i) high/low-temperature cycle. (j) Diagram of the measurement principle of TIM performance based on ASTM D5470 method. (k) The effective thermal resistance of Pad-75-V with varying thicknesses under 10 to 80 Psi.

$$R_{total} = R_{bulk} + R_{contact} \quad (4)$$

With increasing test pressure, the upper and lower surfaces of Pad-75-V establish closer contact with the cold and hot ends of the testing apparatus, thereby reducing $R_{contact}$. Importantly, even under high pressure, Pad-75-V's vertical arrangement structure remains intact, ensuring low R_{bulk}. At a conventional packaging pressure of 50 Psi, the total thermal resistance of Pad-75-V with a thickness of 0.3 mm records an impressively low value of 0.10 °C in^2 W^{-1}.

3.3. Mechanical and electrical properties

Owing to the highly organized and vertically oriented BN structure in conjunction with the remarkable pliability of the silicone matrix, Pad-75-V demonstrates laudable compressibility and resilience, crucial attributes for effective heat transfer under diverse conditions. Fig. 4a visually exemplifies the capacity to nearly revert entirely to its initial state after pressurization and unloading, thereby highlighting its robust compressibility, resilience, and structural stability. The schematic diagram of compression direction was shown in Fig. S7 (ESI†). As illustrated in Fig. 4b, the continuous compression stress–strain curve of Pad-75-V, spanning from 0% to 60%, demarcates three distinct phases: an elastic stage from 0% to 20%, a yield stage from 20% to 45%, and a plastic flow stage from 45% to 60%, corresponding to reversible deformation, partial recovery post-unloading, and irreversible structural deformation, respectively. The stress at 10% strain of Pad-75-V is 5.5 kPa, and the calculated compression modulus amounts to 55 kPa, which is well below than the reported BN/BNNS-based composites (Fig. 4c).[28,47,50–53] A reduced compression modulus implies exceptional adaptability to minor surface irregularities, such as slight unevenness and concavities, thereby augmenting the actual contact area and consequently enhancing thermal conductivity efficiency (Fig. S8, ESI†). Fig. 4d portrays cyclic stress–strain testing of Pad-75-V under various compressive stresses. In the cyclical test at 5% strain, the second cycle's loading curve did not exhibit a high degree of overlap with the first loading curve, yielding a hysteresis phenomenon, primarily attributable to mechanical energy dissipation during the primary compression process. In the following trials, the fourth loading curve displays remarkable alignment with the second loading curve. Throughout subsequent cyclic tests at 10%, 15%, and 20% strains, the fourth cycle's loading curve consistently coincides with the first

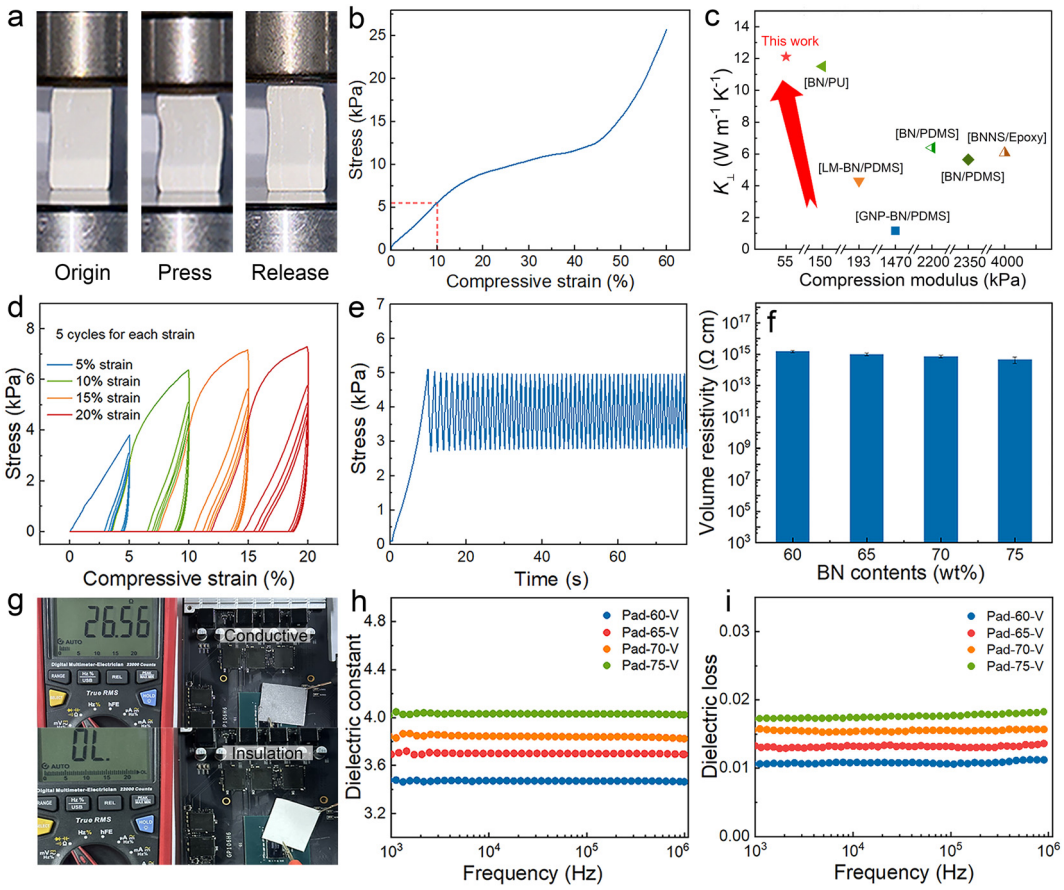

Fig. 4 (a) Digital images of BN/PDMS block post-compression and pre-compression. (b) Compressive stress–strain curves of BN/PDMS block. (c) Performance comparison of Pad-75-V with the reported BN/BNNS composites (Table S3, ESI†). (d) 5%, 10%, 15%, 20% strain cyclic compression curves. (e) Fatigue resistance test curves. (f) Volume resistivity of the Pad with varying BN contents. (g) Insulation performance of Pad-75-V in GPU compared with commercial graphene thermal pad. (h) dielectric constant, (i) dielectric loss of the Pad with varying BN contents.

loading curve, emphasizing the praiseworthy cyclic stability and resilience of Pad-75-V. In addition, 60 cyclic loading tests with a compressive stress of 5 kPa were conducted on Pad-75-V. The curve in Fig. 4e indicates that its structure has good fatigue resistance performance.

Moreover, we performed electrical property assessments on BN thermal pads with various contents (60, 65, 70, and 75 wt%). As depicted in Fig. 4f, the BN thermal pad exhibits exceptional insulating performance, showcasing a volume resistivity surpassing 7×10^{14} Ω cm. To highlight the significance of TIM insulation performance in electronic device thermal management, we positioned Pad-75-V and commercial graphene thermal pad on the GPU and connected them to nearby electronic components to simulate the effects on the circuitry when TIM sliding or overflow. The multimeter's terminals were linked to the GPU and electronic components. Fig. 4g indicates that using Pad-75-V as the TIM carries no risk of short circuit, contrasting with commercial graphene thermal pad. The dielectric constant (Fig. 4h) and dielectric loss (Fig. 4i) of the BN thermal pad register below 4.1 and 0.02, respectively, at ambient temperatures and frequencies ranging from 10^3 to 10^6 Hz. These minimal values signify enhanced transmission speeds of electrical signals while preserving signal purity and stability.

3.4. TIM performance

In order to visually demonstrate the TIM performance of Pad-75-V within actual packaging conditions, a cooling apparatus was constructed to simulate high-power electronic devices. This was achieved by comparing Pad-75-V with a commercial TIM (WT5902, 6 W m^{-1} K^{-1}) as shown in the schematic diagram in Fig. 5a. Both the Pad-75-V and the commercial TIM, with dimensions of $15 \times 15 \times 10$ mm^3, were placed between a ceramic heating element and a radiator, subject to a packaging pressure of 40 Psi controlled *via* a pressure sensor. The surface temperature of the ceramic heating element was monitored in real-time using a thermocouple. Wooden blocks, which served as insulation materials, were positioned between the thermocouple and pressure sensor to

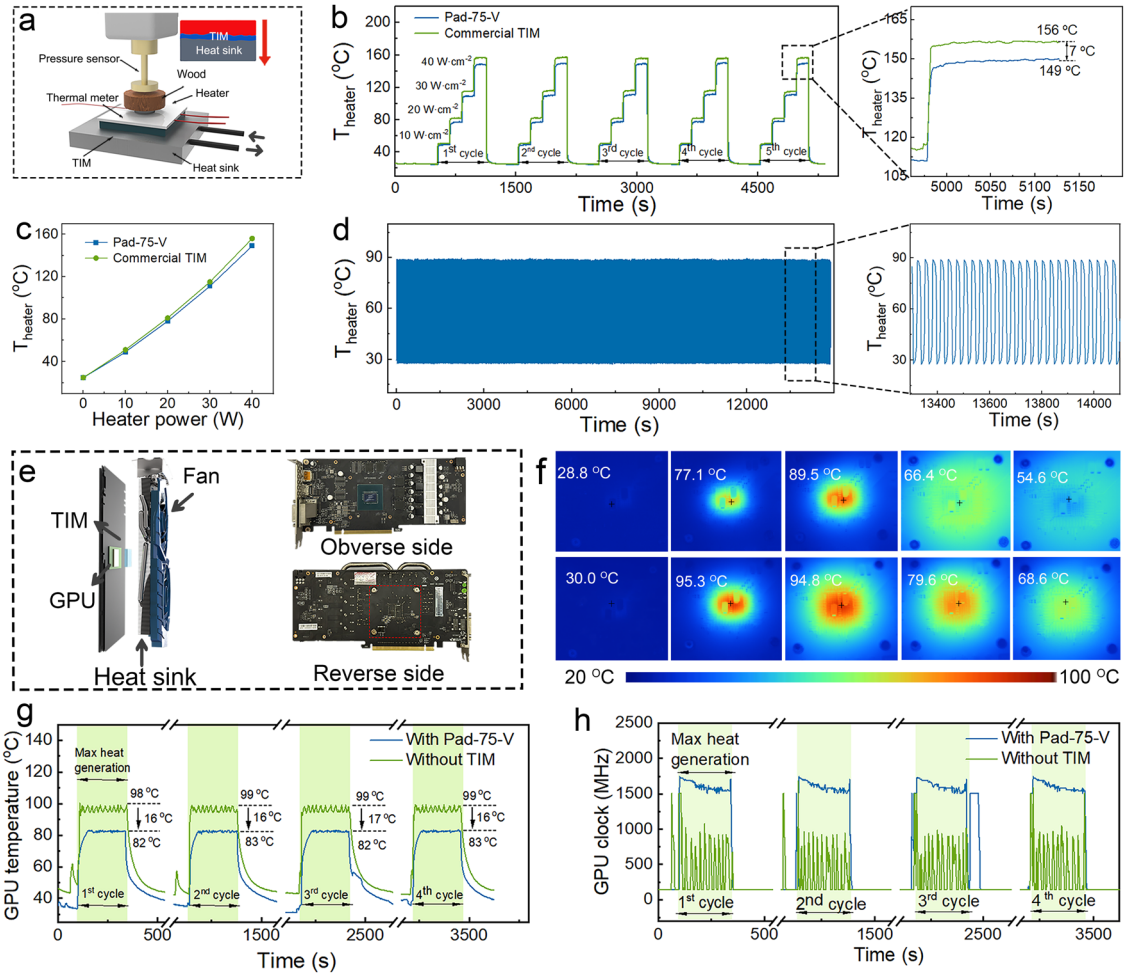

Fig. 5 (a) Diagram of the TIM performance test system. (b) The variation of heater temperature under variable cycle power density. (c) The highest temperature of the heater at different power density. (d) Thermal stability of the cooling system with Pad-75-V as TIM in cyclic heating/cooling tests. (e) Disassembly diagram and obverse and reverse side photos of graphics card. (f) IR images of reverse side of graphics card during full-loading test with Pad-75-V and without TIM. (g) The variation of GPU temperature and (h) clock in full-loading test.

minimize heat loss from the ceramic heating element and ensure the stability of the heat source temperature. When the ceramic heating element was activated, circulating coolant water was directed to the radiator to maintain a stable cold end temperature of 25 °C.

As shown in Fig. 5b, as the power density of the ceramic heating element progressively increased from 10 to 40 W cm^{-2}, its temperature increased sharply and stabilized after five cycles. Under equivalent power density conditions, the temperature of the ceramic heating element utilizing Pad-75-V as a TIM was found to be lower than that using commercial TIM, with the maximum temperature difference reaching 7 °C at a power density of 40 W cm^{-2}. Furthermore, Fig. 5c illustrates that the temperature difference of the ceramic heating element linearly varied with power density, indicating that an increase in power density resulted in a larger temperature difference. These results suggest that the use of Pad-75-V as a TIM provides a more effective heat dissipation effect compared to the commercial TIM.

Additionally, Fig. 5d highlights that Pad-75-V maintains stable heat dissipation performance even after enduring 15 000 s of heating/cooling shock. In order to evaluate the practical application effectiveness of Pad-75-V, a comprehensive study was conducted involving the disassembly and reassembly of a graphics card (GTX 1060ti) with Pad-75-V carefully integrated as TIM between the GPU and heat sink, as portrayed in Fig. 5e. The experiment utilized OCCT software to control the GPU utilization rate, while HWINFO software facilitated real-time monitoring and recording of GPU temperature and frequency. (Fig. S9, ESI†). During 100% graphics card utilization rate, an infrared camera was used to dynamically monitor the real-time temperature on the reverse side of the graphics card. Fig. 5f showed that using Pad-75-V as the TIM resulted in lower temperatures on the reverse side of the graphics card. Fig. 5g presents the outcomes of four cyclic tests, indicating significant advantages with Pad-75-V as the TIM. During standby phases, the core temperature of the GPU exhibited lower levels and a lack of sudden spikes. Under full-loading conditions, the rise in GPU core temperature was more gradual with Pad-75-V, resulting in a maximum temperature reduction of 17 °C compared to scenarios without the TIM. Moreover, after unloading, temperature reduction occurred at an accelerated rate.

Correspondingly, Fig. 5h demonstrates that the presence of Pad-75-V as a TIM ensured consistently stable core frequency of the fully loaded GPU above 1500 MHz, reducing the risk of frequency reduction due to overheating. This consistent performance ensures optimal utilization of the graphics card's processing capabilities, thereby promoting long-term high-performance and stable GPU operation. The reduction in temperature not only enhances the stability of the graphics card but also improves the overall operational stability of adjacent computer components. These findings emphasize the effectiveness of Pad-75-V as a TIM in real-world applications, offering enhanced thermal management and performance optimization for GPU-intensive tasks.

4. Conclusions

In summary, this study employed low molecular weight polydimethylsiloxane (PDMS) and big size boron nitride (BN) to continuously fabricate high-adhesion BN films using a roller curing integrated device. Through a process of stacking, cold pressing, and vertical cutting, we successfully developed a high-performance BN/PDMS composites with remarkable through-plane thermal conductivity (up to 12.11 W m^{-1} K^{-1}), low compression modulus (55 kPa), and total effective thermal resistance (0.16 °C in^2 W^{-1}, 50 Psi). Moreover, the BN-based TIM displayed superior heat dissipation capabilities in comparison to commercial TIM in experimental trials, as evidenced by a 7 °C lower steady-state temperature of the ceramic heating element at a heating power density of 40 W cm^{-2}. These findings contribute valuable insights to the development of high-performance insulating TIMs and open up new possibilities for their widespread implementation in the thermal management of electronic devices.

Author contributions

Rongjie Yang: conceptualization, methodology, investigation, writing original draft; Yandong Wang: methodology, software; Zhenbang Zhang: formal analysis; Kang Xu: methodology; Linhong Li: investigation; Yong Cao: investigation; Maohua Li: software; Jianxiang Zhang: investigation; Yue Qin: software; Boda Zhu: supervision; Yingying Guo: methodology; Yiwei Zhou: supervision, resources; Tao Cai: investigation; Cheng-Te Lin: supervision, resources, funding acquisition; Kazuhito Nishimura: supervision, resources, funding acquisition; Chen Xue: supervision, resources; Nan Jiang: supervision, resources, funding acquisition; Jinhong Yu: conceptualization, resources, writing – review &editing, supervision, project administration, funding acquisition.

Data availability

The data underlying this article will be shared on reasonable request to the corresponding author.

Conflicts of interest

There are no conflicts to declare.

Acknowledgements

The authors are grateful for the financial support by the Science and Technology Base and Talent Project of Guangxi (2022 AC16005) and the National Natural Science Foundation of China (51573201 and 52075527).

Notes and references

1 Y. Chen, H. Zhang, J. Chen, Y. Guo, P. Jiang, F. Gao, H. Bao and X. Huang, *ACS Nano*, 2022, **16**, 14323–14333.

2 Q. He, M. Qin, H. Zhang, J. Yue, L. Peng, G. Liu, Y. Feng and W. Feng, *Mater. Horiz.*, 2024, **11**, 531–544.
3 H. Shi, W. Zhou, Z. Wen, W. Wang, X. Zeng, R. Sun and L. Ren, *Mater. Horiz.*, 2023, **10**, 928–937.
4 W. Dai, X. J. Ren, Q. Yan, S. Wang, M. Yang, L. Lv, J. Ying, L. Chen, P. Tao, L. Sun, C. Xue, J. Yu, C. Song, K. Nishimura, N. Jiang and C. T. Lin, *Nano-Micro Lett.*, 2022, **15**, 9.
5 J. Ying, X. Tan, L. Lv, X. Wang, J. Gao, Q. Yan, H. Ma, K. Nishimura, H. Li, J. Yu, T. H. Liu, R. Xiang, R. Sun, N. Jiang, C. Wong, S. Maruyama, C. T. Lin and W. Dai, *ACS Nano*, 2021, **15**, 12922–12934.
6 M. Cao, Z. Li, J. Lu, B. Wang, H. Lai, Z. Li, Y. Gao, X. Ming, S. Luo, L. Peng, Z. Xu, S. Liu, Y. Liu and C. Gao, *Adv. Mater.*, 2023, **35**, 2300077.
7 Z. Zhang, M. Li, Y. Wang, W. Dai, L. Li, Y. Chen, X. Kong, K. Xu, R. Yang, P. Gong, J. Zhang, T. Cai, C.-T. Lin, K. Nishimura, H. N. Li, N. Jiang and J. Yu, *J. Mater. Chem. A*, 2023, **11**, 10971–10983.
8 M. Li, L. Li, Y. Qin, X. Wei, X. Kong, Z. Zhang, S. Xiong, H. Do, J. C. Greer, Z. Pan, T. Cai, W. Dai, C.-T. Lin, N. Jiang and J. Yu, *J. Mater. Chem. A*, 2022, **10**, 593–601.
9 S. Han, Y. Ji, Q. Zhang, H. Wu, S. Guo, J. Qiu and F. Zhang, *Nano-Micro Lett.*, 2023, **15**, 146.
10 H. Cao, Z. Tan, G. Fan, Q. Guo, Y. Su, Z. Li and D.-B. Xiong, *Composites, Part B*, 2020, **191**, 107965.
11 A. Oluwalowo, N. Nguyen, S. Zhang, J. G. Park and R. Liang, *Carbon*, 2019, **146**, 224–231.
12 X. Li, C. Tan, J. Jiang, S. Wang, F. Zheng, X. Zhang, H. Wang, Y. Huang and Q. Li, *Carbon*, 2021, **177**, 107–114.
13 L. Huang, X. Lv, Y. Tang, G. Ge, P. Zhang and Y. Li, *Polymers*, 2020, **12**, 2126.
14 H. Wang, L. Li, X. Wei, X. Hou, M. Li, X. Wu, Y. Li, C.-T. Lin, N. Jiang and J. Yu, *ACS Appl. Polym. Mater.*, 2020, **3**, 216–225.
15 T. Gao, Z. Yang, C. Chen, Y. Li, K. Fu, J. Dai, E. M. Hitz, H. Xie, B. Liu, J. Song, B. Yang and L. Hu, *ACS Nano*, 2017, **11**, 11513–11520.
16 T. Huang, X. Zhang, T. Wang, H. Zhang, Y. Li, H. Bao, M. Chen and L. Wu, *Nano-Micro Lett.*, 2022, **15**, 2.
17 Q. Li, Z. Xue, J. Zhao, C. Ao, X. Jia, T. Xia, Q. Wang, X. Deng, W. Zhang and C. Lu, *Chem. Eng. J.*, 2020, **383**, 123101.
18 Y. Xue, H. Wang, X. Li and Y. Chen, *Composites, Part A*, 2021, **144**, 106336.
19 X. Zhang, J. Zhang, L. Xia, C. Li, J. Wang, F. Xu, X. Zhang, H. Wu and S. Guo, *ACS Appl. Mater. Interfaces*, 2017, **9**, 22977–22984.
20 K. Zhao, Y. Chen, S. Wei, M. Wang, P. Li, H. Li and X. Zhang, *Ceram. Int.*, 2024, **50**, 19228–19236.
21 L. Chen, C. Xiao, Y. Tang, X. Zhang, K. Zheng and X. Tian, *Ceram. Int.*, 2019, **45**, 12965–12974.
22 J. Zhang, X. Kong, Y. Wang, Z. Zhang, L. Li, K. Xu, M. Li, R. Yang, Y. Zhou, T. Cai, W. Dai, C.-T. Lin, K. Nishimura, Z. Pan, N. Jiang and J. Yu, *J. Mater. Chem. C*, 2023, **11**, 13204–13212.
23 L. Liang, Y. Feng, K. Yang, Z. Wang, Z. Zhang, X. Chen and Q. Chen, *Polymer*, 2024, **290**, 126491.
24 W. Wu, T. Ren, X. Liu, R. Davis, K. Huai, X. Cui, H. Wei, J. Hu, Y. Xia, S. Huang, Z. Qiang, K. Fu, J. Zhang and Y. Chen, *Compos. Commun.*, 2022, **35**, 101309.
25 Y. Wang, A. Gu, Z. Wei, Z. Zhao, H. Cong and C. Yan, *Ceram. Int.*, 2023, **49**, 30248–30256.
26 Z. You, L. Weng, L. Guan, X. Zhang and Z. Wu, *Ceram. Int.*, 2023, **49**, 30204–30213.
27 D. Pan, G. Yang, H. M. Abo-Dief, J. Dong, F. Su, C. Liu, Y. Li, B. Bin Xu, V. Murugadoss, N. Naik, S. M. El-Bahy, Z. M. El-Bahy, M. Huang and Z. Guo, *Nano-Micro Lett.*, 2022, **14**, 118.
28 N. Zhao, J. Li, W. Wang, W. Gao and H. Bai, *ACS Nano*, 2022, **16**, 18959–18967.
29 Z. Yin, J. Guo and X. Jiang, *Compos. Sci. Technol.*, 2021, **209**, 108794.
30 Q. Hu, X. Bai, C. Zhang, X. Zeng, Z. Huang, J. Li, J. Li and Y. Zhang, *Composites, Part A*, 2022, **152**, 106681.
31 H. He, W. Peng, J. Liu, X. Y. Chan, S. Liu, L. Lu and H. Le Ferrand, *Adv. Mater.*, 2022, **34**, 2205120.
32 X. Cai, Y. Liu, T. Yang, X. Dong, X. Zhang, Z. Jiang, A. Chou, T. Gao and X. Zhang, *J. Appl. Polym. Sci.*, 2021, **138**, 50575.
33 X. Liu, Q. Han, D. Yang, Y. Ni, L. Yu, Q. Wei and L. Zhang, *ACS Omega*, 2020, **5**, 14006–14012.
34 X. Zhang, J. Yi, Y. Yin, Y. Song and C. Xiong, *Diamond Relat. Mater.*, 2021, **117**, 108485.
35 X. Wu, W. Liu, L. Ren and C. Zhang, *e-Polymers*, 2020, **20**, 510–518.
36 Y. Wang, W. Wu, D. Drummer, C. Liu, W. Shen, F. Tomiak, K. Schneider, X. Liu and Q. Chen, *Mater. Des.*, 2020, **191**, 108698.
37 Z. Wu, J. Dong, X. Li, X. Zhao, C. Ji and Q. Zhang, *Composites, Part B*, 2023, **266**, 111001.
38 M. A. Kashfipour, R. S. Dent, N. Mehra, X. Yang, J. Gu and J. Zhu, *Compos. Sci. Technol.*, 2019, **182**, 107715.
39 X. Wang and P. Wu, *ACS Appl. Mater. Interfaces*, 2019, **11**, 28943–28952.
40 Y. Yao, Z. Ye, F. Huang, X. Zeng, T. Zhang, T. Shang, M. Han, W. Zhang, L. Ren, R. Sun, J. B. Xu and C. P. Wong, *ACS Appl. Mater. Interfaces*, 2020, **12**, 2892–2902.
41 M. Donnay, S. Tzavalas and E. Logakis, *Compos. Sci. Technol.*, 2015, **110**, 152–158.
42 J. Hou, G. Li, N. Yang, L. Qin, M. E. Grami, Q. Zhang, N. Wang and X. Qu, *RSC Adv.*, 2014, **4**, 44282–44290.
43 D. Lee, S. Lee, S. Byun, K.-W. Paik and S. H. Song, *Composites, Part A*, 2018, **107**, 217–223.
44 N. Yang, C. Xu, J. Hou, Y. Yao, Q. Zhang, M. E. Grami, L. He, N. Wang and X. Qu, *RSC Adv.*, 2016, **6**, 18279–18287.
45 S. Zuo, Y. Lan, J. Luo, F. Zhou, L. Xu, S. Xie, X. Wei, L. Zhou, L. Ma, X. Li and C. Yin, *ACS Omega*, 2022, **7**, 43273–43282.
46 C. Lei, Y. Zhang, D. Liu, X. Xu, K. Wu and Q. Fu, *Compos. Sci. Technol.*, 2021, **214**, 108995.
47 H. Niu, H. Guo, L. Kang, L. Ren, R. Lv and S. Bai, *Nano-Micro Lett.*, 2022, **14**, 153.

48 Q. Song, W. Zhu, Y. Deng, F. Hai, Y. Wang and Z. Guo, *Composites, Part A*, 2019, **127**, 105654.
49 S. Xu, H. Liu, Q. Li, Q. Mu and H. Wen, *J. Mater. Chem. C*, 2016, **4**, 872–878.
50 K. Yang, X. Yang, Z. Liu, K. Li, Y. Yue, R. Zhang, F. Wang, X. Shi, J. Yuan, N. Liu, G. Wang, Z. Wang and G. Xin, *ACS Appl. Mater. Interfaces*, 2023, **15**, 28536–28545.
51 J. Han, G. Du, W. Gao and H. Bai, *Adv. Funct. Mater.*, 2019, **29**, 1900412.
52 J. Wang, S. Wang, X. Cheng, R. Lv, Y. Luo, S. Wang, X. Liu, B. Zhou, R. Sun, Y. Liu, X. Zeng and Z. Yu, *Compos. Commun.*, 2024, **47**, 101881.
53 J. Zhang, H. Wang, T. Zhang, X. Sun, Y. Meng, C. Ma, T. Zhang, N. Lu, C. Liu and Y. Zeng, *Compos. Sci. Technol.*, 2023, **233**, 109915.